



RESEARCH ARTICLE

10.1002/2014JD022848

Key Points:

- Recent Arctic sea-ice reduction shifts the AO to be more negative phase
- Associated negative AO pattern brings continental cooling in the NH mid-latitude
- Positive feedback process to ice reduction cools mid-latitudes and warms Arctic

Correspondence to:

T. Nakamura,
nakamura.tetsu@ees.hokudai.ac.jp

Citation:

Nakamura, T., K. Yamazaki, K. Iwamoto, M. Honda, Y. Miyoshi, Y. Ogawa, and J. Ukita (2015), A negative phase shift of the winter AO/NAO due to the recent Arctic sea-ice reduction in late autumn, *J. Geophys. Res. Atmos.*, *120*, doi:10.1002/2014JD022848.

Received 15 NOV 2014

Accepted 25 MAR 2015

Accepted article online 28 MAR 2015

A negative phase shift of the winter AO/NAO due to the recent Arctic sea-ice reduction in late autumn

Tetsu Nakamura^{1,2}, Koji Yamazaki^{1,2}, Katsushi Iwamoto^{1,3}, Meiji Honda³, Yasunobu Miyoshi⁴, Yasunobu Ogawa¹, and Jinro Ukita³

¹National Institute of Polar Research, Tachikawa, Japan, ²Hokkaido University, Sapporo, Japan, ³Niigata University, Niigata, Japan, ⁴Kyushu University, Fukuoka, Japan

Abstract This paper examines the possible linkage between the recent reduction in Arctic sea-ice extent and the wintertime Arctic Oscillation (AO)/North Atlantic Oscillation (NAO). Observational analyses using the ERA interim reanalysis and merged Hadley/Optimum Interpolation Sea Surface Temperature data reveal that a reduced (increased) sea-ice area in November leads to more negative (positive) phases of the AO and NAO in early and late winter, respectively. We simulate the atmospheric response to observed sea-ice anomalies using a high-top atmospheric general circulation model (AGCM for Earth Simulator, AFES version 4.1). The results from the simulation reveal that the recent Arctic sea-ice reduction results in cold winters in mid-latitude continental regions, which are linked to an anomalous circulation pattern similar to the negative phase of AO/NAO with an increased frequency of large negative AO events by a factor of over two. Associated with this negative AO/NAO phase, cold air advection from the Arctic to the mid-latitudes increases. We found that the stationary Rossby wave response to the sea-ice reduction in the Barents Sea region induces this anomalous circulation. We also found a positive feedback mechanism resulting from the anomalous meridional circulation that cools the mid-latitudes and warms the Arctic, which adds an extra heating to the Arctic air column equivalent to about 60% of the direct surface heat release from the sea-ice reduction. The results from this high-top model experiment also suggested a critical role of the stratosphere in deepening the tropospheric annular mode and modulation of the NAO in mid to late winter through stratosphere-troposphere coupling.

1. Introduction

The recent decrease in Arctic sea-ice extent (SIE) is a marked signature of global warming in the troposphere, which is likely a combined result of anthropogenic radiative forcing by increasing greenhouse gases, natural variability, and feedbacks within the Earth's ice-ocean-atmosphere coupled system on a decadal timescale [Serreze *et al.*, 2007, 2009; Comiso *et al.*, 2008; Schweiger *et al.*, 2008; Kay *et al.*, 2011]. Previous studies have examined the atmospheric response to changes in Arctic SIE to gain a better understanding of the underlying feedback mechanisms and interactions of the Arctic ice-ocean-atmosphere coupled system. Anomalously cold winters in the mid-latitudes over Eurasia have been linked to an atmospheric response to Arctic summer sea-ice reduction [Francis *et al.*, 2009; Honda *et al.*, 2009; Petoukhov and Semenov, 2010; Inoue *et al.*, 2012; Liu *et al.*, 2012; Tang *et al.*, 2013]. The dynamical processes associated with this remote response have been identified in both observation-based analysis and atmospheric general circulation model (AGCM) experiments. Francis *et al.* [2009] found that changes in Northern Hemisphere (NH) atmospheric circulation such as the weakening of the polar jet stream are associated with a reduction in Arctic sea ice. Honda *et al.* [2009] showed that the stationary Rossby wave response to the increased turbulent heat flux resulting from summer Arctic-ice reduction intensifies the wintertime Siberian high that brings cold air outbreaks.

Previous studies have noted that Arctic sea ice is affected by atmospheric variability associated with the Arctic Oscillation (AO)/Northern Hemisphere Annular Mode (NAM) [e.g., Rigor *et al.*, 2000, 2002; Ogi *et al.*, 2008, 2010; Ogi and Yamazaki, 2010; Stroeve *et al.*, 2011], which is a dominant mode of Northern Hemisphere atmospheric variability [Thompson and Wallace, 1998, 2000]. Other large-scale variations, such as the dipole pattern in the Arctic, also have an impact on Arctic sea ice [Wu *et al.*, 2006; Maslanik *et al.*, 2007; Stroeve *et al.*, 2007; Holland *et al.*, 2008; L'Heureux *et al.*, 2008; Wang and Overland, 2009]. On the other hand, some studies have reported that the negative phase of the AO/NAM appears as a response to Arctic sea-ice reduction in AGCM experiments with prescribed sea-ice or Sea Surface Temperature (SST)

©2015. The Authors.

This is an open access article under the terms of the Creative Commons Attribution-NonCommercial-NoDerivs License, which permits use and distribution in any medium, provided the original work is properly cited, the use is non-commercial and no modifications or adaptations are made.

conditions [Alexander et al., 2004; Deser et al., 2004; Magnúsdóttir et al., 2004; Yamamoto et al., 2006; Kim et al., 2014; Mori et al., 2014]. Recently, a relationship between summer Arctic ice reduction and the negative phase of the AO/NAM and North Atlantic Oscillation (NAO) signals in winter has been identified [Jaiser et al., 2012; Liu et al., 2012]. Observation-based studies have reported that the negative trends in the AO/NAM and NAO are related to the decreasing trend in Arctic sea ice from summer to autumn [Overland and Wang, 2010; Hopsch et al., 2012; Rinke et al., 2013] and the increasing trend in Eurasian snow cover [Cohen et al., 2012]. Results from numerical simulations using atmosphere-ocean coupled models suggest that Arctic sea-ice variability and the modulation of the AO/NAM are linked [Sokolova et al., 2007; Cohen et al., 2012].

Recognizing a potentially critical role of this link in the NH climate system, the primary goal of this study is to determine the underlying processes connecting Arctic sea-ice variability, the associated atmospheric response, and modulation of the AO/NAM and the NAO. Our understanding of the atmospheric response to Arctic sea-ice variability is often hindered by a large amount of internal atmospheric variability [Deser and Phillips, 2009; Screen et al., 2013]. Noting this difficulty, we evaluate changes in the probability distribution of the AO/NAM index related to sea-ice reduction while taking internal atmospheric variability into account. We have used an AGCM to address these issues by conducting sensitivity experiments with changing boundary conditions representing sea-ice variability. In particular, we used a model with a sufficiently high model top to allow a reasonable representation of stratospheric variability. This is because the behavior of the AO/NAM and the NAO in the troposphere is related to the strength of the polar vortex aloft [Baldwin and Dunkerton, 1999, 2001; Ambaum and Hoskins, 2002; Polvani and Waugh, 2004]. In this paper, we first examine the observed atmospheric variability in the NH associated with Arctic sea-ice variability. Next, we investigate the climatological impacts of recent Arctic ice reduction using AGCM experiments, and finally, we examine the modulation of the simulated AO/NAM through an analysis of the model results.

2. Data and Indices

2.1. Sea Surface Temperature (SST) and Sea-Ice Concentration (SIC)

We used the merged Hadley-National Oceanic and Atmospheric Administration (NOAA)/Optimum Interpolation (OI) Sea Surface Temperature (SST) and Sea-Ice Concentration (SIC) [Hurrell et al., 2008] datasets for the period 1979–2011. We defined a sea-ice area (SIA) index as $SIC (\%) \times \text{grid area (m}^2\text{)}$ integrated northward of 65°N for each calendar month, representing interannual variations of the Arctic sea ice.

The same data were also used as boundary conditions for sensitivity experiments using an AGCM. To examine the influences of the recent Arctic ice reduction, we used 5-year monthly varying climatologies for an *Early* period (1979–1983) and a *Late* period (2005–2009). As an example of changes in SIC and thus converted grid-wise averaged sea-ice thickness (SIT) (see section 2.4 for the detailed discussion regarding the conversion of SIC and SIT and the relationship with the turbulent heat flux), Figure 1a shows SIT anomalies between the late and early periods in September. Figures 1b and 1c show SIT anomalies in November and January, respectively. The SIT shows large sea-ice reductions in the East Siberian Sea in September, in the Barents-Kara Sea and the Bering Strait in November, and in the Barents Sea, the Nordic Sea, and the Sea of Okhotsk in January. Figures 1d–1f show regression coefficients of detrended SIT anomaly against the detrended and normalized SIA index in September, November, and January, respectively. Spatial patterns of *Late-minus-Early* anomalies are similar to the regressions, while magnitudes of *Late-minus-Early* anomalies are about four times larger than the regression. We thus deduce that similar physical processes dominate the atmospheric responses to the Arctic sea-ice changes on interannual and decadal timescales.

2.2. ERA Interim Reanalysis

We used monthly mean data from the European Centre for Medium-Range Weather Forecasts (ECMWF) ERA interim reanalysis for the period 1979–2012 [Dee et al., 2011]. Data were averaged over 3-month periods (e.g., December, January, and February; DJF) to reduce noise caused by the high-frequency internal variability of atmospheric fields. We used linear regression to evaluate the impacts of sea-ice variations over interannual timescales, in which the ERA interim data and SIA index for the period 1979–2012 were detrended before regressing atmospheric variables on the SIA index.

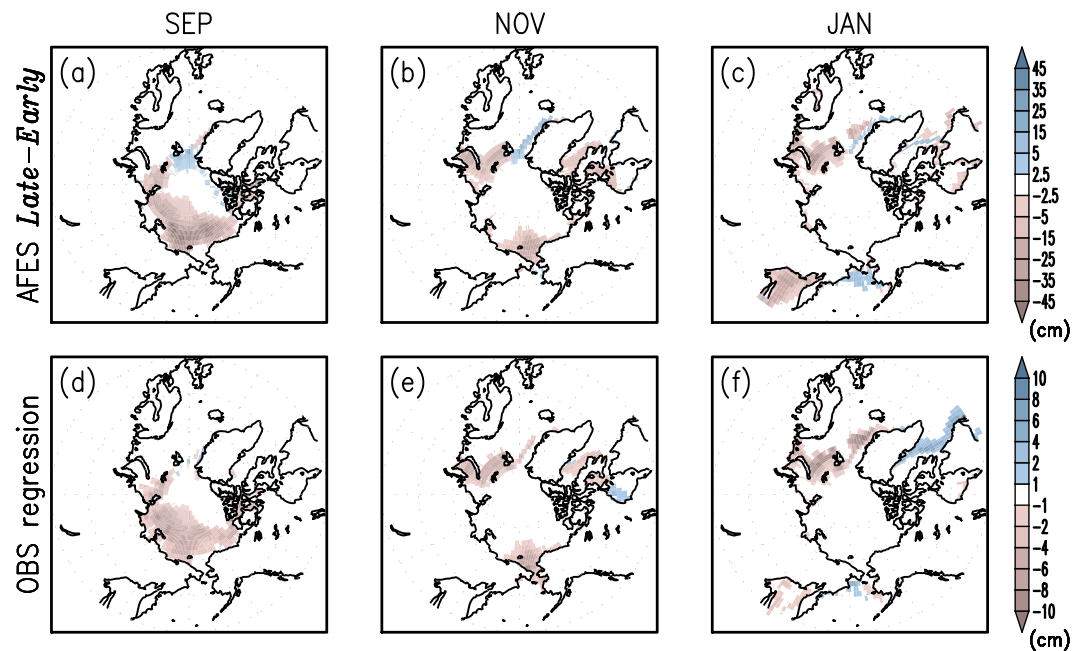


Figure 1. (a–c) SIT (cm) anomalies of *Late* (2005–2009) minus *Early* (1979–1983) periods in September, November, and January, respectively. (d–f) Sign-reversed regression coefficients of detrended SIT anomaly against normalized sea-ice area index in September, November, and January, respectively. The signs of the regression coefficients have been reversed so that they correspond to the decrease in Arctic sea ice.

2.3. Annular Mode Indices

We used the AO and NAO indices provided by the National Oceanic and Atmospheric Administration (NOAA) Climate Prediction Center (CPC) (<http://www.esrl.noaa.gov/psd/data/climateindices>). The indices were averaged for 3 months prior to use. Furthermore, we calculated the empirical orthogonal functions (EOF) of 3-month mean geopotential height at 500 hPa (Z500) northward of 30°N. Area weighting was applied to the height fields before carrying out EOF analysis. The spatial pattern of the primary mode was quite similar to the Z500 anomaly regressed on the AO index in the individual 3-month mean. The EOF1 score of this Z500-EOF was used as an annular mode index (Z500-EOF1 score) in the middle troposphere.

2.4. Model and Simulations

We used the AGCM for Earth Simulator (AFES) [Ohfuchi *et al.*, 2004, 2007; Enomoto *et al.*, 2008; Kuwano-Yoshida *et al.*, 2010] version 4.1 with triangular truncation at horizontal wavenumber 79 (T79; approximately 1.5° horizontal resolution), and with 56 vertical levels and the model top of about 60 km. The AFES version 4.1 used here is a major update of the version previously used by Honda *et al.* [2009], as the horizontal resolution and model top are both higher (increasing from T42 to T79 and 30 to 60 km, respectively). Our model does not treat SIC directly; instead, each model grid cell is either treated as being ice-covered or ice-free. To allow our model to represent a reasonable amount of the turbulent heat flux associated with variable SIC, SIC data were converted into SIT. We assumed a maximum ice thickness in the Arctic of 50 cm so that SIC from 0% to 100% was linearly converted into SIT from 0 to 50 cm. We then set all grid cells where converted SIT was less than 5 cm to have no ice (i.e., 0 cm). Although 50 cm is much thinner than a typical Arctic SIT value, the turbulent heat flux over sea ice is simulated reasonably well due to the large reduction in the conductive heat flux through sea-ice thicker than 30–50 cm [Maykut, 1982]. Observation-based estimates of the turbulent heat flux in the Arctic are about -10 W m^{-2} over the fully sea-ice-covered region and about $300\text{--}320 \text{ W m}^{-2}$ over the open-water region [Maykut, 1982; Renfrew *et al.*, 2002]. The simulated heat flux in the Arctic of our model is comparable with observations (see Appendix A). Perpetual model runs were performed with boundary conditions of mean seasonal cycles of the global SST and SIT. Other external forcings were all fixed as follows: 380 ppmv for CO₂, 1.8 ppmv for CH₄, and the monthly climatological mean

Table 1. Description of the Perpetual Model Simulations^a

	Integration period (years)	SST	SIT
<i>CNTL</i>	60	<i>Early</i>	<i>Early</i>
<i>N.ICE</i>	60	<i>Early</i>	<i>Late</i>

^a“Early” (“Late”) indicates that the boundary conditions were monthly averaged SST or SIT for a 5-year period covering 1979–1983 (2005–2009).

O₃ for 1979–2011 obtained from the Japanese 25-year Reanalysis (JRA-25)/ Japan Meteorological Agency (JMA) Climate Data Assimilation System (JCDAS) reanalysis data [Onogi *et al.*, 2007]. Default values of aerosol and incident solar radiation were used.

The control run (*CNTL*) was performed with a 5-year monthly varying climatology of SST and SIT for the *Early* period (1979–1983). A perturbed run (*N.ICE*) used the same SST as *CNTL* but SIT climatology for the *Late* period (2005–2009). The two cases are summarized in Table 1. Both runs used the same initial conditions (the January 1979 monthly mean from JRA-25/JCDAS). We carried out 60-year integrations after an 11-year spin-up. The differences between the 60-year averages of *CNTL* and *N.ICE* (*N.ICE* minus *CNTL*) were examined. By this experimental design, only the sea-ice difference is responsible for atmospheric differences without any influences from other external forcings such as SST variations. Daily mean outputs of all variables were averaged over 3 months, and we focused on the boreal winter (DJF).

3. Results

3.1. Observational Evidence for an Ice-Atmosphere Linkage

First, we examined observational evidence for a relationship between wintertime atmospheric and Arctic sea-ice variations. As sea ice has a much longer memory than the atmosphere, we calculated the lag-correlations between the DJF mean AO index and the SIA index in the preceding months. After detrending both the AO index and SIA index, the correlations were 0.14, 0.28, 0.48, and 0.26 for the SIA in September, October, November, and December, respectively. The maximum correlation, between November SIA and the DJF mean AO index, exceeds the 95% ($r=0.35$) confidence level. The time series of November SIA and the DJF mean AO and NAO indices are shown in Figure 2. Both of the DJF-averaged AO and NAO indices are significantly correlated with the November SIA, at both interannual and decadal timescales (e.g., the negative trends after 1989).

Figure 3 (top row) shows anomalies of 3-month mean geopotential height at 500 hPa (Z500) from October–November–December (OND) to January–February–March (JFM) regressed on the time series of the November Arctic sea-ice area. Note that the sign is reversed so that anomalies shown are associated with a decrease in Arctic sea ice. Most of the regressed anomalies show positive anomalies in the Arctic Ocean region but negative anomalies at mid-latitudes. This structure of the geopotential height anomaly resembles the negative phase of the AO/NAM pattern. Consistent with this result, regressions of sea level pressure (SLP) anomalies shown in Figure 3 (middle row) have persistent positive anomalies in the Arctic Ocean region and negative anomalies at mid-latitudes. In comparison, Figure 4 shows sign-reversed correlation

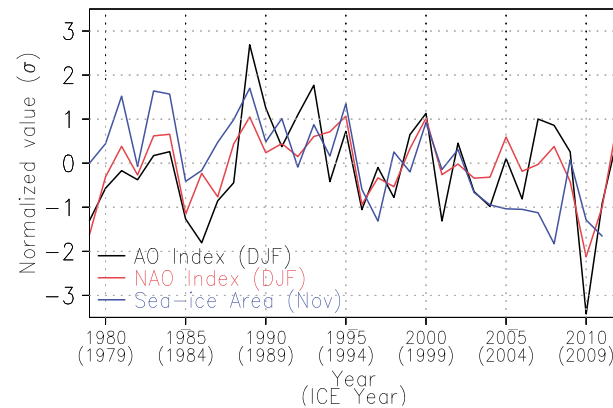


Figure 2. Time series of DJF-averaged AO and NAO indices (obtained from NOAA CPC at <http://www.esrl.noaa.gov/psd/data/climateindices/>), together with the normalized time series of SIA index in the previous November.

coefficients of the November SIA index with the AO index from August–September–October (ASO) to March–April–May (MAM) (solid black line). The correlations are negative, with large magnitudes from -0.42 in ASO to -0.53 in DJF, and then rapidly decrease to a minimum in February–March–April (FMA). While the correlations of Z500-EOF1 score (dashed black line) are similar to those of the AO index, high negative correlations of the NAO index (gray line) occur in wintertime. This strong relationship between the annular mode from late summer to mid-winter and November sea-ice variability suggests that the summer annular mode may affect the summer-to-autumn Arctic sea ice and the autumn Arctic sea ice may affect the winter annular

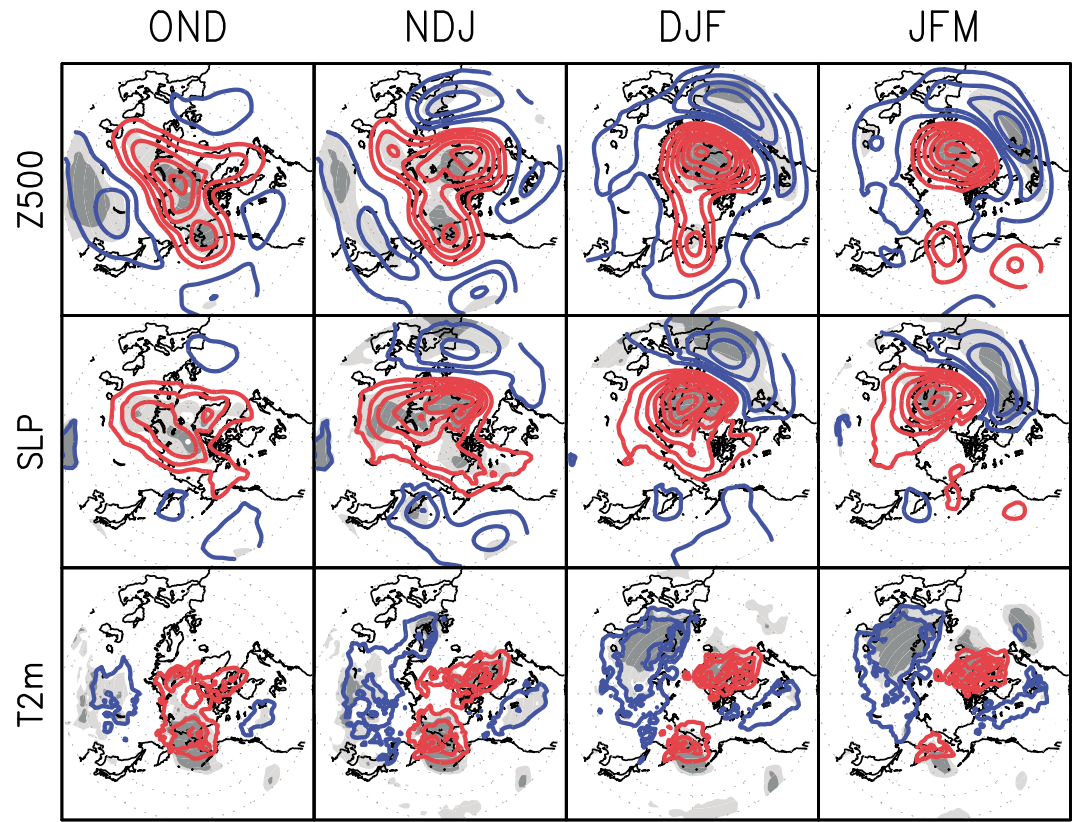


Figure 3. (Top) 3-month mean geopotential height anomalies at 500 hPa (Z500) during (from left to right) OND, NDJ, DJF, and JFM. These anomalies are lag regression coefficients against the normalized SIA index in November. Note that the sign of the coefficients is reversed so that red (blue) corresponds to positive (negative) anomalies when Arctic sea ice decreases. The contour interval is 5 m, and the zero line is omitted. Light and heavy shading indicate statistical significance of over 95% and 99%, respectively. (Middle) Regression coefficients of sea level pressure with a contour interval of 0.5 hPa. (Bottom) Regression coefficients of 2-m temperature with a contour interval of 0.5 K.

mode, because the annular mode signal does not persist beyond the season. While the negative anomalies of Z500 in central to eastern Siberia are significant in early winter (OND and November–December–January; NDJ), those in Europe and the North Atlantic are significant in late winter (NDJ–JFM) as seen in Figure 3, top row. Such a shift in the spatial pattern from Siberia to the North Atlantic is also found in the SLP anomalies (Figure 3, middle row). During OND, positive anomalies in the Arctic Ocean extend toward Eurasia around 90°E. Then, from NDJ to JFM, negative anomalies in the North Atlantic gradually develop as extensions of the positive anomalies around 90°E gradually vanish.

Anomalies in the temperature at 2-m height (T2m) also show this shift (Figure 3, bottom row). That is, during OND and NDJ, cold anomalies are found in eastern Siberia associated with the high-pressure anomalies in northern Siberia (i.e., intensification of the Siberian high), and during DJF and JFM, cold anomalies are found in eastern Europe.

These results indicate that sea-ice variability in late autumn is strongly related to the AO/NAM-like variations from late summer to mid-winter. Furthermore, interannual variations in wintertime atmospheric fields show a gradual shift from negative (positive)

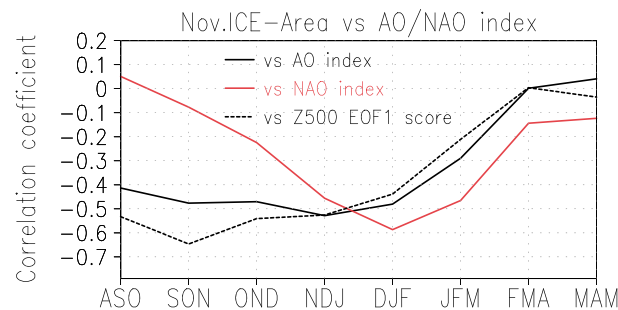


Figure 4. Changing correlation between the November SIA index and 3-month mean AO/NAO indices and Z500-EOF1 score from ASO to MAM. As in Figure 1, signs of the correlation coefficients have been reversed so that they correspond to decreases in Arctic sea ice.

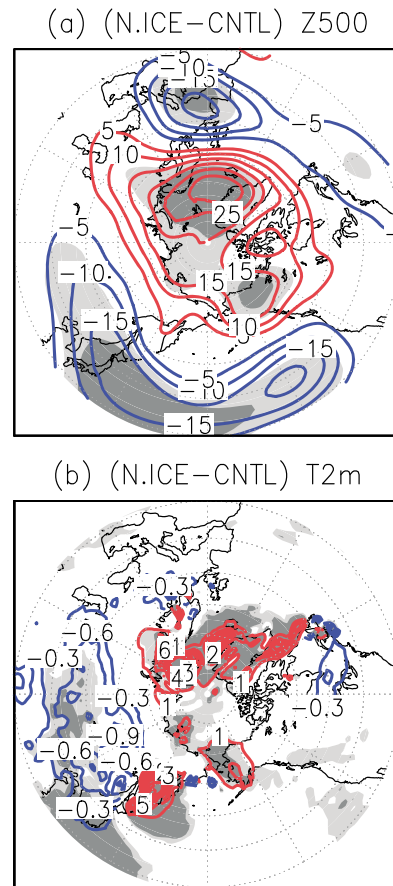


Figure 5. (a) Anomalies of geopotential height at 500 hPa in DJF for the *N.ICE* run relative to the *CNTL* run. Contours indicate the differences in meters. The contour interval is 5 m, and the zero line is omitted. Light and heavy shading indicate statistical significance (*t*-test) at the 95% and 99% confidence levels, respectively. (b) As for Figure 5a but for 2-m temperature. Contour interval is 1.0 (0.3) K for positive (negative) anomalies.

mid-latitudes, corresponding to the Z500 anomalies. Cold anomalies in Siberia through East Asia are large in size and statistically significant, while those in Europe and eastern North America are smaller and less significant.

Next, we examine to what extent the model results spatially resemble the regression maps of ERA interim data upon the November SIA index (Table 2). The spatial correlations of simulated Z500 anomalies in DJF (northward of 30°N) with the ERA interim anomalies in NDJ and DJF are significantly high, with coefficients of 0.86 and 0.69, respectively. The spatial correlations of simulated T2m are similar but generally

AO-like signals in early winter to negative (positive) NAO-like signals in mid-winter associated with the decrease (increase) in November sea-ice extent. The above results indicate the possible influence of Arctic sea-ice reduction in late autumn on the recent negative trend in winter annular modes. However, the lag correlation analysis does not rule out a possibility that sea ice is not a controlling factor and other factors such as SST variations in the tropics affect both circulation and sea ice with different lagging timescales, thereby leading to an apparent lag relationship between sea ice and circulation. In order to examine if sea ice alone affects atmospheric circulation in a manner consistent with our observations, we specifically design our numerical experiment with the prescribed sea ice in high and low states while anything else being fixed. Thus, our experiment provides information as to how changes in the NH sea ice alone affect the atmosphere.

3.2. Climatological Impact of Recent Ice Reduction
3.2.1. Model Results and Comparisons With Observations

In this section, we analyze the differences between the *CNTL* and *N.ICE* runs to evaluate the climatological impact of the recent Arctic sea-ice reduction. We also compare model results with fields regressed upon the November SIA index from the ERA interim reanalysis data.

We first examine Z500 and T2m because they are essential variables that represent atmospheric variability in the troposphere and near the surface, respectively. Figure 5a shows the Z500 anomalies of *N.ICE* with respect to *CNTL*. Positive anomalies are found over the Arctic Ocean, while negative anomalies are found at mid-latitudes in the Pacific and Atlantic Ocean. Although changes in sea ice in the Arctic Ocean are solely responsible for the anomalous atmospheric fields, significant anomalies are found in mid-latitudes. A wave-train-like structure along the Eurasian Arctic coast (i.e., Europe-Barents-Siberia) resembles the Eurasian (EU) pattern [Wallace and Gutzler, 1981; Ohhashi and Yamazaki, 1999]. Figure 5b shows that the T2m anomalies are positive in the Arctic Ocean and the Sea of Okhotsk, and negative in the

Table 2. Spatial Correlation Coefficients Between Model Fields (see Figures 5a and 5b) and ERA Interim Anomaly Fields in NDJ and DJF Regressed on the November SIA Index (top and bottom columns of Figure 3)^a

	500 hPa geopotential height		2-m temperature	
	ERA in NDJ	ERA in DJF	ERA in NDJ	ERA in DJF
<i>N.ICE</i> minus <i>CNTL</i> in DJF	0.86	0.69	0.28	0.15

^aThe correlations were calculated using anomaly fields northward of 30°N.

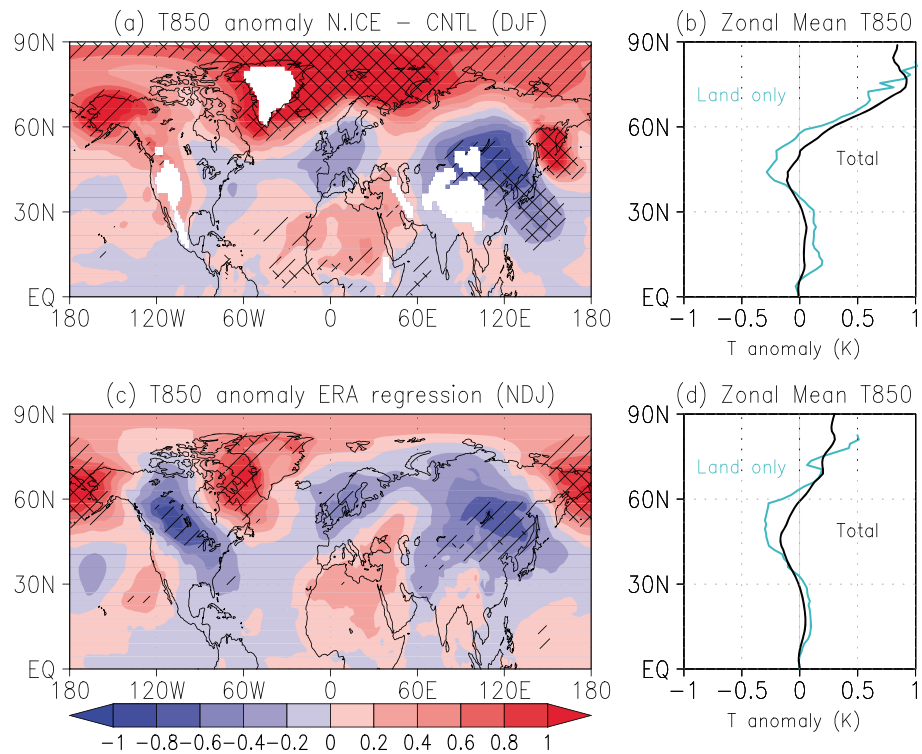


Figure 6. (a) DJF mean temperature anomalies at 850 hPa of *N.ICE* against *CNTL*. Hatched and double-hatched areas indicate statistical significance (*t*-test) at the 95% and 99% confidence levels, respectively. (b) Zonal mean temperature anomalies. Black and light blue lines indicate the global mean and land-only mean, respectively. (c and d) As for Figures 6a and 6b, but for the regressed field of ERA interim in NDJ upon November SIA index. Values corresponding to -1.0σ of SIA index are shown.

substantially weaker. The stronger correlations for Z500 suggest a stronger role for tropospheric dynamics rather than a direct near-surface response to boundary forcing. The high correlations of Z500 anomalies suggest that the model accurately simulates the atmospheric response to the sea-ice reduction. Note that the correlation is slightly higher for NDJ than for DJF. In the remainder of this section, we use the regression fields in NDJ for comparison with the model results.

Figures 6a and 6b show the NH temperature response in *N.ICE* relative to *CNTL*, and its zonal mean, respectively. Significant cold anomalies are found in eastern Siberia and warm anomalies over the Arctic Ocean and the Sea of Okhotsk. The zonal mean temperature response shows large warm anomalies in the polar region. In the mid-latitudes, while the zonal mean temperature response shows small anomalies, anomalies averaged only over land are clearly negative. The area-weighted temperature response over the NH mid-latitudes (30–60°N) is nearly zero, -0.01 K. However, averaging only over the land area gives -0.10 K, with a minimum of -0.29 K at 44.1°N. In comparison, Figure 6c presents regressed fields of observed NDJ mean temperatures at 850 hPa associated with the normalized time series of November sea-ice area. Warm anomalies in the Arctic and cold anomalies over mid-latitude land are also found. Continental cold anomalies are located in North America, Europe, and eastern Siberia. Simulated spatial pattern of the cold anomalies resemble the observed pattern, although for the simulation, there are no significances in North America and less in Europe. The area-weighted temperature response averaged over the NH mid-latitudes (30–60°N) is -0.09 K, with a minimum of -0.17 K at 45.0°N; averaged only over land, this becomes -0.18 K, with a minimum of -0.30 K at 49.5°N. Those results strongly suggest that the recent sea-ice reduction contributes to the cooling of the NH continents.

3.2.2. Stationary Rossby Wave Response and Associated Modulation of the Meridional Circulation

Having recognized the statistical relationships between Arctic sea-ice reduction and the atmospheric response in both geopotential height and temperature fields, we next consider possible mechanisms for the occurrence of cold anomalies over NH land. Figure 7 shows DJF-averaged 3D temperature advection

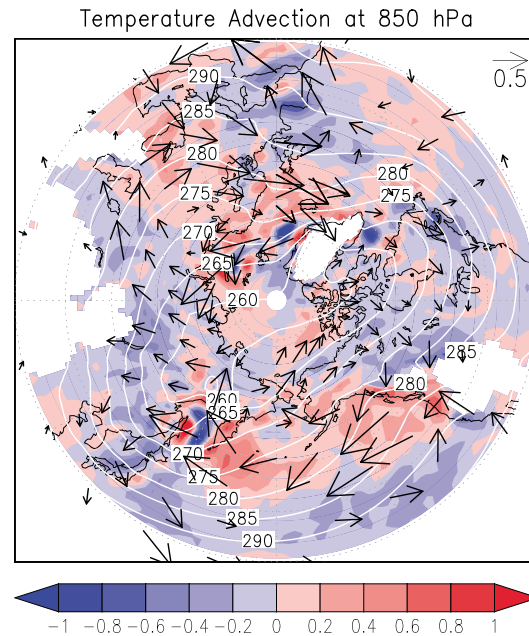


Figure 7. DJF-averaged climatology of temperature (K, contours), vectors of the horizontal wind anomaly (arrows), and 3D temperature advection (K d^{-1} , shading) at 850 hPa. The climatology and anomalies are calculated as $(CNTL \text{ plus } N.ICE)/2$ and $N.ICE \text{ minus } CNTL$, respectively. Temperature advection is obtained from the products of 3D wind anomalies and the climatological potential temperature gradient. Note that the vertical wind anomalies are not shown but are taken into account for temperature advection. The arrow length corresponding to 0.5 m s^{-1} is indicated in the top-right corner of the panel.

of the Rossby wave train that originates in the Arctic region can be seen in eastern Siberia. The disturbance in eastern Siberia (around Lake Baikal, $110^\circ\text{E } 50^\circ\text{N}$) originates from an upward propagation of the Rossby wave activity associated with turbulent heat flux anomalies over the Barents Sea. Figure 8b shows geopotential height anomalies at 300 hPa (Z_{300}) from the *N.ICE* experiment (*N.ICE* minus *CNTL*) and corresponding WAF. The wave activity propagates from the Barents Sea region to eastern Siberia where cyclonic anomalies are found. Figure 8c shows vertical-meridional cross-sections of geopotential height anomalies, and zonal and vertical components of the WAF along the brown line in Figure 8b. The Rossby wave activity propagates upwards and eastwards from the wave source near the surface in the Arctic region (northward of 65°N). This is similar to the result of *Honda et al.* [2009], who found cyclonic anomalies in eastern Siberia formed by a stationary Rossby wave response to the sea-ice reduction in the Barents Sea. The pathway of WAF in eastern Siberia is located west of the climatological troughs (Figure 9a) and is collocated with the southeastward extension of the jet stream. This is consistent with the idea that the Rossby wave train prefers to propagate along a waveguide where the meridional gradient of the absolute vorticity is large (red hatching in Figure 9b). Therefore, this result implies that Arctic ice reduction induces a modulation of the climatological planetary wave, which is accompanied by changes in the meridional circulation that are related to the heat exchange between the Arctic and mid-latitudes.

We next examine changes in the meridional circulation based on transformed Eulerian mean (TEM) diagnosis in an attempt to estimate the feedback of these circulation changes onto the Arctic climate. Figure 10a shows DJF zonal mean wind anomalies of *N.ICE* with respect to *CNTL*. A dipole pattern from the weakened subpolar jet ($50\text{--}70^\circ\text{N}$) and intensified subtropical jet (around 30°N) is evident in the troposphere, and the former connects with the weakened polar vortex in the stratosphere (around 70°N). Figure 10b shows anomalies in the Eliassen-Palm (EP) flux [*Andrews and McIntyre*, 1976] and its divergence. Upward wave propagation is enhanced in the lower to middle troposphere, and the upper tropospheric zonal flow at high latitudes

anomalies (*N.ICE* minus *CNTL*) caused by climatological temperature advected by anomalous winds. Advection of cold air from the climatological cold core by the anomalous wind produces the near-surface temperature anomalies over eastern Siberia, North America, and western Europe. The anomalous wind at 850 hPa corresponds to a geostrophic relationship with the geopotential height anomalies in the upper levels (e.g., 500 hPa in Figure 5a). The upper-level geopotential anomalies (which are strongly associated with potential vorticity anomalies) induce low-level wind anomalies [*Lau and Holopainen*, 1984; *Lau and Nath*, 1991] and are consistent with the results of *Honda et al.* [2009].

We next examine how the Arctic ice reduction affects changes in the atmospheric circulation in the middle to upper troposphere. To achieve this, following *Honda et al.* [2009], we used the wave activity flux (WAF) developed by *Takaya and Nakamura* [2001], which indicates the 3D group velocity of a quasi-geostrophic wave packet and thus the propagation of the stationary Rossby wave activity. Figure 8a shows anomalous fields of the *N.ICE* experiment (*N.ICE* minus *CNTL*) including the turbulent heat flux (i.e., the sum of sensible and latent heat fluxes from the surface to the atmosphere), the vertical component of the WAF at 700 hPa, and the horizontal vectors of the WAF at 300 hPa. The southward propagation

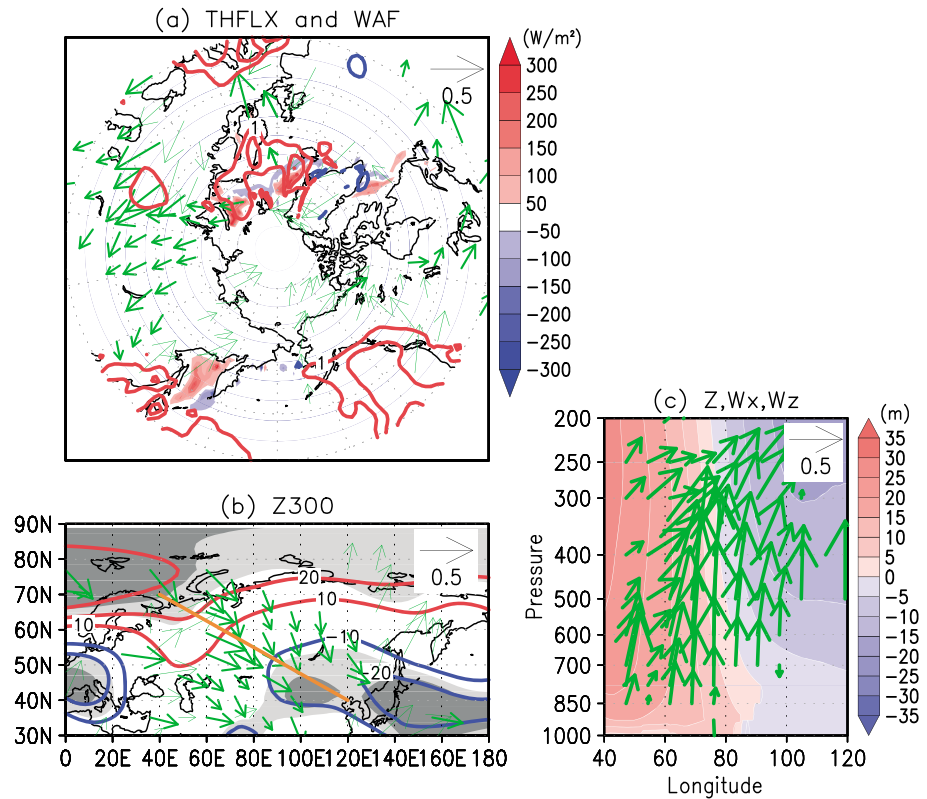


Figure 8. DJF-averaged anomalies of *N.ICE* with respect to the *CNTL* run. (a) Shading, contours, and arrows indicate turbulent heat flux ($W m^{-2}$; i.e., sensible plus latent heat, upward positive), the vertical component of wave activity flux ($10^{-2} m^2 s^{-2}$) at 700 hPa, and the horizontal wave activity flux vector ($m^2 s^{-2}$) at 300 hPa, respectively. The arrow length corresponding to $0.5 m^2 s^{-2}$ is indicated in the top-right corner of each panel. Note that the horizontal wave activity fluxes in the southward (northward) direction are drawn as thick (thin) arrows. (b) Geopotential height anomalies at 300 hPa. Contours and shading are the same as in Figure 5a. Associated wave activity fluxes are shown by green arrows. (c) Vertical cross-sections of geopotential height anomalies and the zonal and vertical components of wave activity flux along the brown line in (b). The vertical component of the vectors is multiplied by a factor of 600.

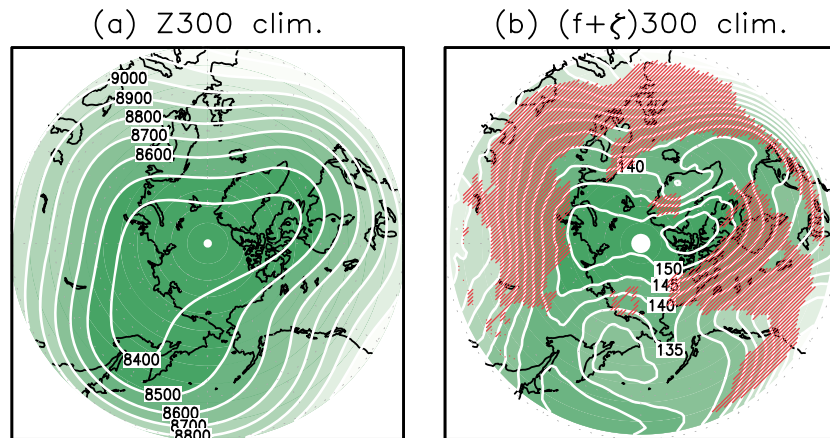


Figure 9. DJF-averaged climatologies of (a) geopotential height (m) and (b) absolute vorticity ($10^6 s^{-1}$) at 300 hPa. The climatology is defined as the 120-year average of the *CNTL* and *N.ICE* runs. Meridional gradients of the absolute vorticity exceeding $10^{-8} s^{-1} km^{-1}$ are hatched in red in Figure 9b.

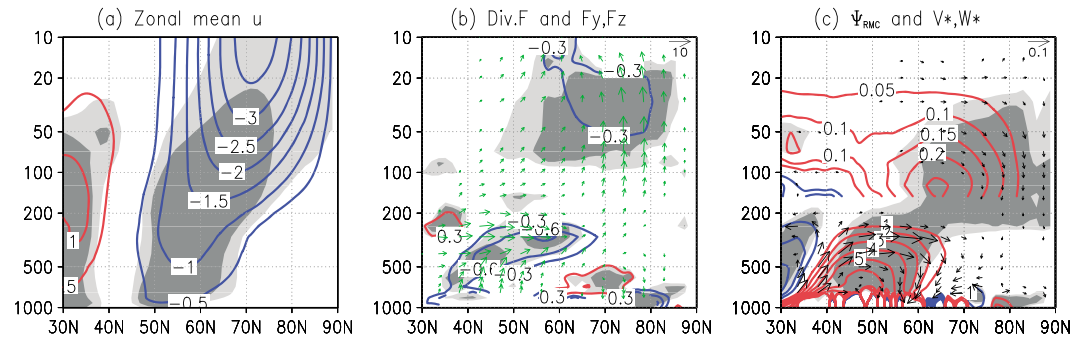


Figure 10. DJF-averaged zonal mean anomalies of *N.ICE* with respect to the *CNTL* run. (a) Zonal wind anomalies (m s^{-1}). (b) EP flux ($\text{m}^2 \text{s}^{-2}$, green arrows) and its divergence ($\text{m s}^{-1} \text{day}^{-1}$, contours). Magnitude of EP flux was standardized by pressure (p/p_0) and earth's radius (6.37×10^6). (c) Residual mean circulation (m s^{-1} , black arrows) and stream function ($10^{10} \text{m}^2 \text{s}^{-1}$, contours). For all panels, light and heavy shading indicates statistical significance at the 95% and 99% confidence levels, respectively. For Figures 10b and 10c, the vertical component of the vectors is multiplied by a factor of 200, and arrow lengths corresponding to $10 \text{m}^2 \text{s}^{-2}$ and 0.1m s^{-1} are displayed in the top-right corner of Figures 10b and 10c, respectively.

(around 50–60°N at 300 hPa) is decelerated by the resulting wave drag. Furthermore, upward wave propagation is evident at high latitudes in the stratosphere, and this decelerates the stratospheric polar vortex (around 70°N and 50–20 hPa). Figure 10c shows the anomalous residual mean circulation associated with the calculated EP flux divergence. To balance the zonal flow deceleration due to the anomalous wave drag, a northward residual circulation is induced in the upper troposphere (40–60°N between 400 and 300 hPa) accompanied by upward motion in the mid-latitudes (30–40°N) and downward motion in the high latitudes (50–70°N). In the stratosphere, similar northward residual circulation (around 70°N and 50–20 hPa) and associated downward motion (northward of 70°N and 200–50 hPa) are evident. Figure 11a shows the longitudinal distribution of DJF-averaged anomalies of eddy momentum flux ($u'v'$) at 300 hPa (*N.ICE* minus *CNTL*). Here the eddy is defined as the anomaly from a zonal mean of a daily variable, according to the TEM formulation. Negative anomalies of the eddy momentum flux corresponding to northward EP flux anomalies are found in southern Europe and northeastern Asia. Figure 11b shows the longitudinal distribution of the anomalous eddy heat flux (vT') at the 500 hPa level. Positive anomalies corresponding to upward EP flux anomalies are found in Europe and northeastern Asia, and negative

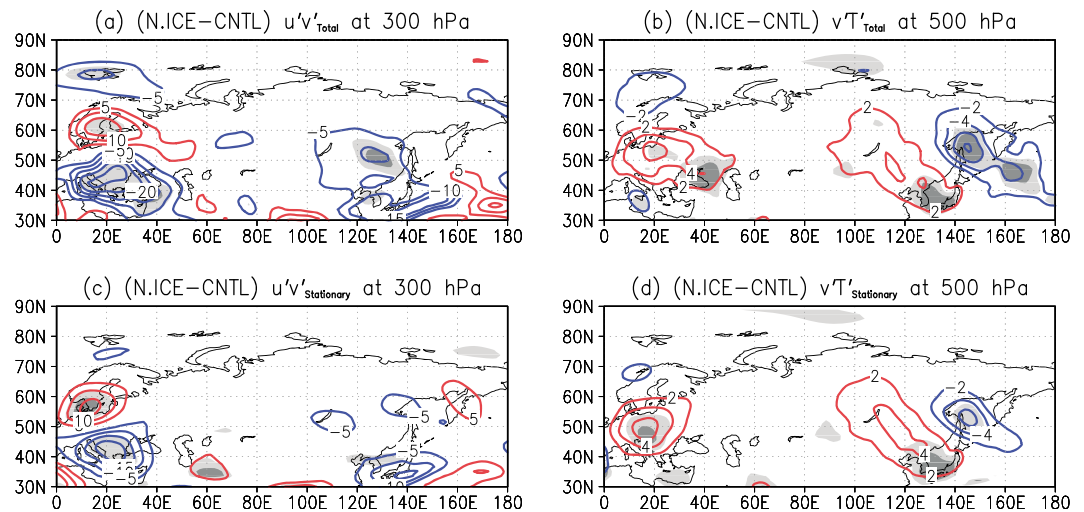


Figure 11. (a) As for Figure 5a but for the eddy momentum flux ($u'v'$) obtained from daily mean data. An eddy is defined as an anomaly from the zonal mean field according to the TEM formulation. The units are $\text{m}^2 \text{s}^{-2}$. (b) Eddy heat flux (vT' , K m s^{-1}). (c and d) As for Figures 11a and 11b, but for fluxes obtained from DJF mean data. Only the fluxes due to the stationary eddies are shown.

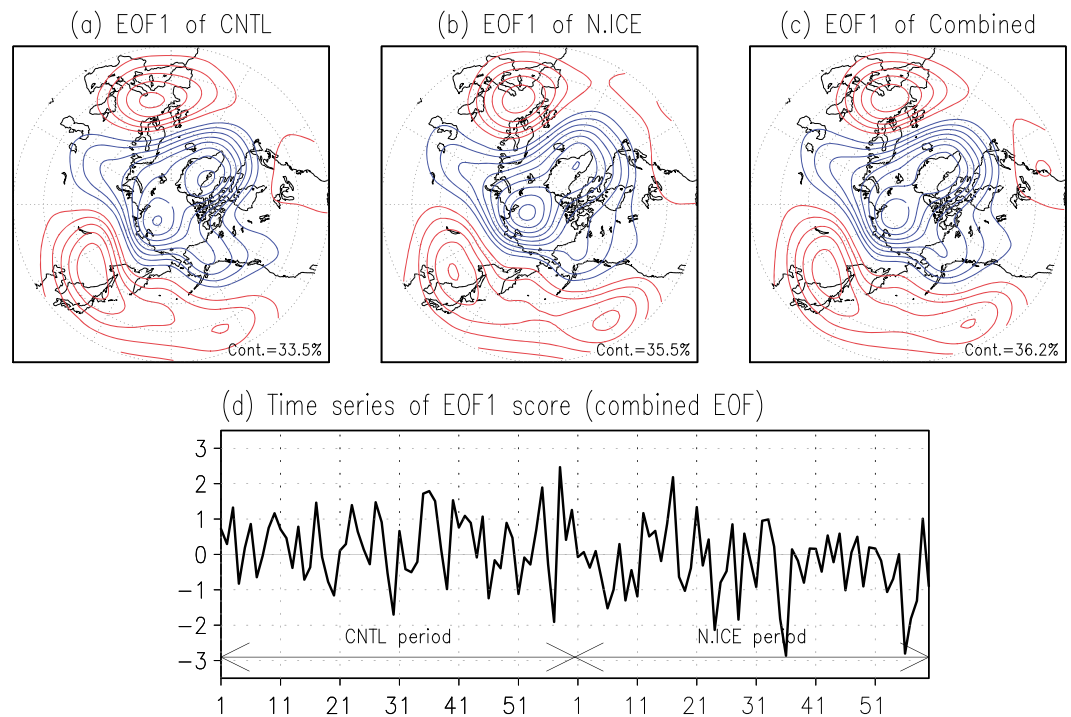


Figure 12. DJF-averaged geopotential height anomalies at 500 hPa for (a) *CNTL*, (b) *N.ICE*, and (c) *CNTL + N.ICE*. Anomalies are obtained from regressions against the normalized EOF1 score, and thus, patterns are almost the same to EOF1 loading pattern. Contour interval is 5 m, with zero omitted. The contribution of EOF1 is indicated at the bottom right of each panel. (d) Standardized EOF1 scores for the combined EOF. The left and right halves of Figure 12d correspond to the 60-year periods of *CNTL* and *N.ICE*, respectively.

anomalies corresponding to downward EP flux anomalies are found in the Sea of Okhotsk. Figures 11c and 11d show the eddy momentum and heat fluxes due to the stationary eddies (i.e., anomalies from the zonal mean of DJF-averaged variables), respectively. The flux anomalies due to the stationary eddies are similar to the total fluxes. This implies that the contributions of flux anomalies due to stationary eddies are dominant whereas the transient contribution is relatively small. This result suggests that, in mid-latitudes, the stationary wave response to sea-ice reduction is likely to be a driver of the anomalous meridional circulation.

The adiabatic processes associated with the anomalous meridional circulation shown in Figure 10c cool the mid-latitudes and warm the polar region throughout the troposphere, suggesting that changes in the mean flow associated with the modulation of the planetary wave act as a positive feedback on the impacts of Arctic sea-ice reduction. We estimated the heating rate induced by the residual mean vertical motion (w^*) in the troposphere (850–300 hPa; see Appendix B). The heating rate averaged over the polar region (northward of 60°N) was 2.27 W m^{-2} , and that averaged over the mid-latitudes (30–60°N) was -1.59 W m^{-2} . This heating rate induced by the secondary circulation amounts to about 63% of the direct heat release from the ice reduction into the atmosphere, which is 3.61 W m^{-2} , obtained from the turbulent heat flux anomaly integrated over the Arctic and divided by the area northward of 60°N.

3.2.3. Modulation of the AO/NAM

As shown in section 3.2.2, the vertical motion induced by ice reduction warms the Arctic and cools mid-latitudes. Such an anomalous meridional circulation caused by stationary wave drag is accompanied by a weakening of the polar vortex, which shows variability that is strongly related to the AO/NAM [Limpasuvan and Hartmann, 2000]. We estimated the contribution of Arctic sea-ice reduction to the AO/NAM signals. To do this, we applied an EOF analysis to the 3-month mean Z500 data from the 60-year results of the *CNTL* and *N.ICE* runs, and to the Z500 data from *N.ICE* combined with those from *CNTL* (i.e., a total sample size of 120 years, hereafter referred to as *CNTL + N.ICE*). Using this combined EOF analysis, we evaluated the modulation of AO/NAM as a response to recent sea-ice reduction.

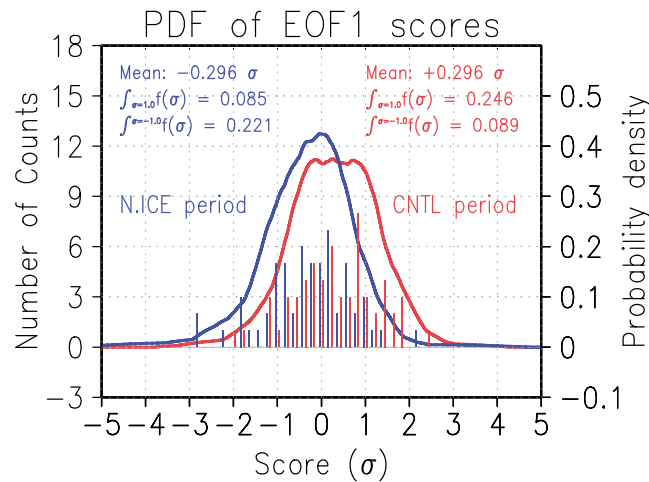


Figure 13. Histogram of the EOF1 score from the combined EOF (0.2σ bins); red and blue bars indicate the CNTL and N.ICE periods, respectively. The horizontal axis shows scores for the center of each bin. The vertical axis on the left hand side indicates the number of counts for each bin. Lines indicate the probability density function (PDF) estimated from the EOF1 score for the CNTL (red) and N.ICE (blue) periods, respectively. The vertical axis on the right-hand side indicates probability density. The mean score and the integral of the PDF above (below) 1.0σ (-1.0σ) are shown in the panel in the colors corresponding to CNTL and N.ICE (red and blue, respectively).

Figures 12a–12c show regressions of DJF mean Z500 anomalies against EOF1 scores from CNTL, N.ICE, and CNTL + N.ICE, respectively. Because the anomalies themselves used for EOF were regressed, the patterns emulate the EOF1 loading pattern. The structures of the horizontal pattern in the three EOF1s do not differ notably. The score of the combined EOF1 can be used to simplify the quantification of the modulation of the primary mode. Figure 12d shows the time series of the EOF1 scores of CNTL + N.ICE. The score shifts to be more negative from the CNTL period to the N.ICE period. The difference between these two periods is 0.593σ , which exceeds the 99% significance level. This shift indicates the changes in probability distribution of the primary mode in the atmosphere due to changes in the boundary conditions (i.e., the AO/NAM shift to the negative phase is associated with the Arctic sea-ice reduction). This is

consistent with the cold anomalies in mid-latitudes shown in Figure 6. Due to the meandering of the high latitude jet stream, cold air outbreaks from the Arctic to the mid-latitudes occur more frequently during the negative phase of AO/NAM than during the positive phase.

For a more quantitative estimate of the modulation of the primary mode, we examined the probability density function (PDF) of the EOF1 score using the nonparametric density estimation technique [Kimoto and Ghil, 1993]. Figure 13 shows histograms and associated PDFs of combined EOF1 scores for the CNTL and N.ICE periods. The probability density for positive scores is larger over the CNTL period than over the N.ICE period. The probabilities of positive scores larger than 1.0σ were 24.6% and 8.5% for the CNTL and N.ICE periods, respectively. On the other hand, the probabilities for scores less than -1.0σ were 8.9% and 22.1% for the CNTL and N.ICE periods, respectively. Furthermore, while the PDF of CNTL is skewed to the right (skewness = 0.175), that of N.ICE is skewed to the left (skewness = -0.096). This finding supports the more frequent appearances of a strong negative phase of the AO/NAM during the N.ICE period. The results also indicate that strong positive AO/NAM events occur less frequently (<50%) in association with a negative shift of the AO/NAM due to the Arctic sea-ice reduction, and vice versa.

Finally, we consider the seasonal evolution of the impact of sea-ice reduction on NH climatic fields. The top panels of Figure 14 compare the Z50 and Z500 anomalies of the N.ICE run with the CNTL run from the OND to JFM periods. In the stratosphere, while positive anomalies are only evident in far-eastern Russia in the OND and NDJ periods, large positive anomalies are found in the Arctic surrounded by negative anomalies in the mid-latitudes in the DJF and JFM periods. This indicates the weakening of the polar vortex in mid to late winter. In comparison, negative AO-like anomalies appear throughout the troposphere and strengthen toward late winter. The simulated seasonal evolution in the troposphere resembles that observed. In particular, in both observations and simulation, the dipole pattern in the north Atlantic resembling the negative NAO is more apparent in DJF and JFM than in OND and NDJ. Such a deepening of the annular mode is also indicated by the seasonal evolution of the EOF1 scores shown in the bottom panel of Figure 14. The EOF1 negative scores gradually increase in magnitude from late autumn (ASO) to mid-winter (DJF) and return toward near-zero in spring (MAM). This resembles the observed evolution of the annular modes (Figure 4), although we note that observational results are based on the AO/NAM index (EOF of 1000 hPa pressure level), while the simulated results are based on the EOF of Z500. The simulated

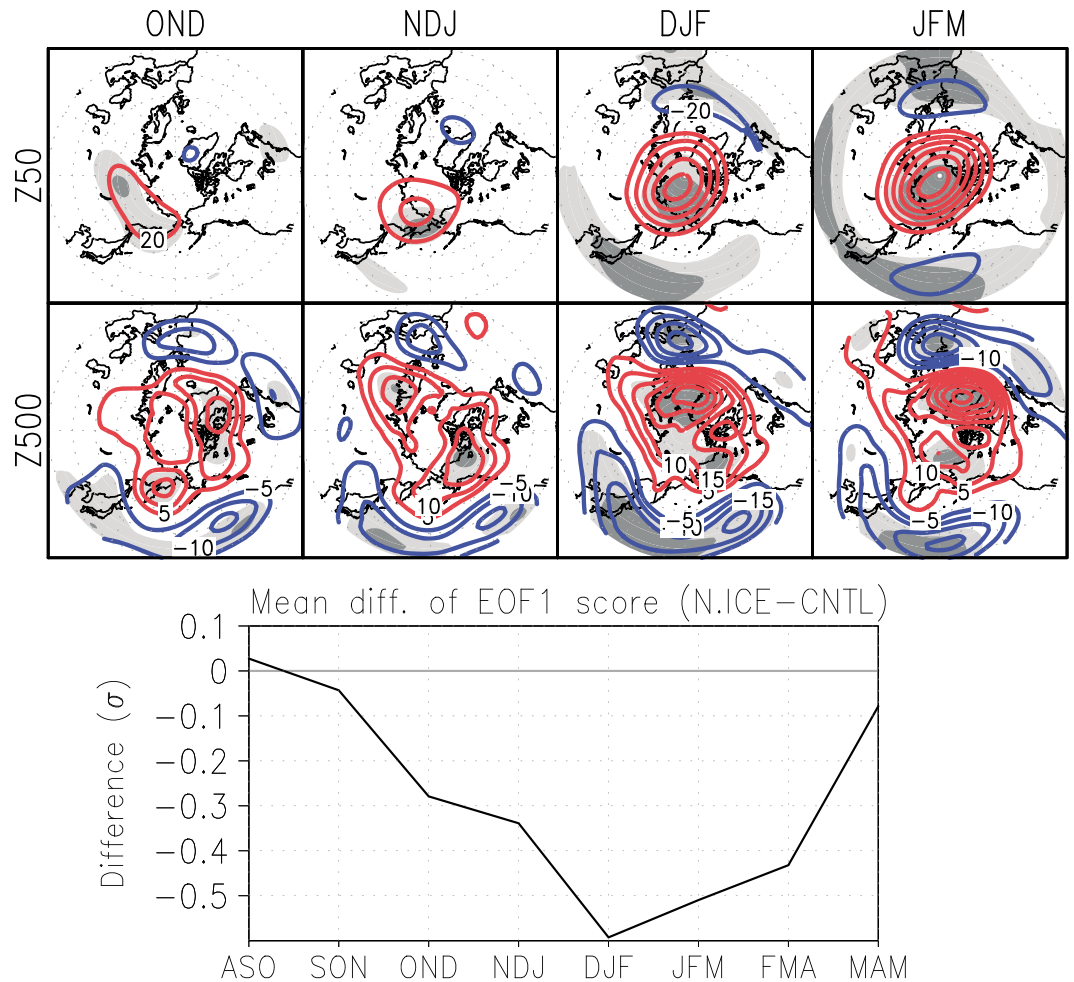


Figure 14. (Top) Geopotential height anomalies of *N.ICE* with respect to *CNTL* in OND, NDJ, DJF, and JFM at 50 hPa (upper row) and 500 hPa (lower row). Contours and shading intervals are as in Figure 5a. (Bottom) Time series of the mean difference of the EOF1 scores (i.e., *N.ICE* minus *CNTL*).

weakening of the polar vortex in the stratosphere in the mid to late winter implies a role of the stratosphere in deepening the tropospheric annular mode. Figures 15a and 15b show daily anomalies (*N.ICE* minus *CNTL*) of zonal mean zonal wind at 60°N and temperature at 80°N, respectively. Significant deceleration of the polar night jet and a corresponding stratospheric warming anomaly are seen at the end of January. The signals propagate downward and penetrate into the troposphere in February. Figure 15c shows a time-latitude cross-section of the vertical component of the EP flux anomaly through the lower stratosphere (100 hPa). A positive anomaly exists around 70°N at the end of December and around 50°N in January, indicating an intensification of the propagation of the planetary wave from the troposphere to the stratosphere. The intensified upward propagation of the planetary wave causes the deceleration of the polar night jet and the polar stratospheric warming, which later propagate downward to the troposphere. The simulated behavior is consistent with downward propagation of the stratospheric signature induced by the planetary wave modulation [Baldwin and Dunkerton, 1999, 2001].

4. Discussion

4.1. Winter Annular Modes and November Sea Ice

In section 3.1, we showed that the wintertime AO/NAM- and NAO-like signals are strongly related to Arctic sea-ice variability in November. Many studies have reported a significant relationship between the Arctic summer sea-ice loss, in particular September sea ice, and the negative trend of AO/NAM based on both

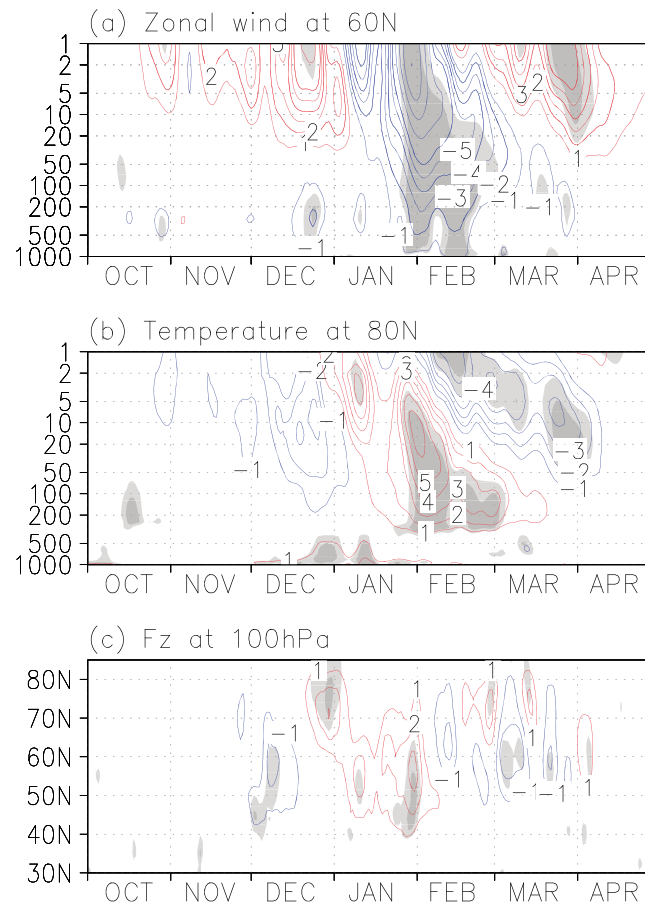


Figure 15. Winter seasonal evolution of anomalies of *N/ICE* with respect to *CNTL* for (a) zonal mean zonal wind at 60°N (m s^{-1}), (b) zonal mean temperature at 80°N (K), and (c) vertical component of EP flux ($10^4 \text{ m}^2 \text{ s}^{-2}$) at 100 hPa. Contour and shading intervals are as in Figure 5a.

response to NH sea-ice reduction (*N/ICE* case) shows geopotential height anomalies similar to the EU pattern. Surface temperature anomalies associated with the EU pattern show continental cooling structures mainly in the eastern Siberia similar to the regression fields from the ERA interim reanalysis dataset (Figure 6). The spatial correlations between the model responses and the ERA interim anomalies are significant. However, those comparisons were made between observationally derived regression fields and different climatological fields in the simulations, reflecting the difficulty in determining the atmospheric responses to sea-ice reduction directly from the observations. We keep in mind that the observed changes in the atmosphere of the *Late* (2005–2009) minus *Early* (1979–1983) periods largely reflect the global warming effect, and thus, the impacts of ice reduction were significantly masked (not shown here).

Our model showed AO/NAO-like responses to the sea-ice anomalies that were defined within the realistic range (Early and Late periods). The appearance of AO/NAO-like anomalies associated with sea-ice variation is consistent with the observational results and recent model studies [Petoukhov and Semenov, 2010; Kim et al., 2014; Mori et al., 2014]. However, some of the previous studies with AMIP-type simulation, in which interannual variation of SST impacts on the Arctic atmosphere, did not show strong sensitivity of the sea-ice reduction on the AO/NAO pattern. Such varying results among model simulations in terms of an appearance of AO/NAO may be due to controls by other external forcings including SST variations.

Our model also showed a possible influence of the stratospheric AO signal on the tropospheric sea-ice-AO linkage (section 3.2.3, Figure 15). This indicates an inherent advantage of the high-top model to study underlying mechanisms for the sea-ice-AO linkage.

observations [Overland and Wang, 2010; Hopsch et al., 2012; Jaiser et al., 2012; Liu et al., 2012; Rinke et al., 2013] and numerical simulations [Sokolova et al., 2007; Cohen et al., 2012; Liu et al., 2012]. Based on our results, the autumn Arctic sea-ice variability is more strongly related to the winter AO/NAM. This is reasonable because Arctic sea-ice variability is large in the Barents Sea in autumn and the East Siberian Sea in summer, and thus, the associated surface turbulent heat flux anomalies over the Arctic Ocean are much larger in autumn than in summer. As we discuss below, this supports a possible mechanism for the modulation of the AO/NAM. Furthermore, the November sea-ice variation is also related to the summer AO/NAM. This is consistent with Ogi et al. [2008, 2010], who showed that the summer-to-autumn persistence of the sea-ice anomaly is related to the summer AO.

4.2. Climatological Impacts of Recent Sea-Ice and SST Anomalies

In section 3.2, we showed the climatological impact of recent ice reduction on the NH climate by comparing results from the model experiments. The winter atmospheric

4.3. Possible Mechanism for Modulation of the AO/NAM

The negative phase shift in the primary AO/NAM-like mode is found in both the model experiments and the reanalysis data. The modulation of the AO/NAM results from a combination of two dynamical processes in steps. In the first step, the stationary Rossby wave response to sea-ice reduction in the Barents Sea appears in eastern Siberia in early to mid-winter (Figures 3 and 14), as suggested by previous studies [Francis *et al.*, 2009; Honda *et al.*, 2009; Liu *et al.*, 2012; Tang *et al.*, 2013]. Later, an annular-mode-like pattern, with anticyclonic anomalies in the polar region and cyclonic anomalies in the mid-latitudes, becomes more apparent in mid and late winter. This results from the second step of the dynamical process, in which the stationary eddies associated with the Rossby wave response in mid-latitudes induce an anomalous meridional circulation that cools the mid-latitudes and warms the polar region (Figure 10), further leading to the negative AO-like anomalies. Because the AO/NAM is a dominant mode of the internal variation of the NH atmosphere, the sea-ice reduction does not always induce the negative phase of AO/NAM. However, because the preferred waveguide of the winter climatological jet stream is located near the anomalous turbulent heat flux around the Barents Sea (Figures 8 and 9), these dynamical processes often occur in association with the sea-ice reduction. As a result, the probability of a negative phase of the AO/NAM tends to increase.

Our results in the model experiments are consistent with previous studies that showed a negative AO-like response to the Arctic sea-ice reduction [Alexander *et al.*, 2004; Deser *et al.*, 2004; Magnusdottir *et al.*, 2004]. On the basis of our findings, we argue that the stationary Rossby response to sea-ice reduction and its consequent modulation of the stratospheric circulation may explain the AO-projected component of the response to the sea-ice variation shown by Magnusdottir *et al.* [2004] and Deser *et al.* [2004]. Honda *et al.* [1996, 1999], Alexander *et al.* [2004], and Yamamoto *et al.* [2006] suggested that sea-ice changes in the Sea of Okhotsk generate a wave-train-like response that propagates toward North America. Our model simulation does not show such a response to the Okhotsk sea-ice reduction; rather, the responses look more zonal. This might suggest that the dynamical feedback (e.g., eddy-mean flow interaction) to the Arctic anticyclonic anomaly due to the additional warming in the Arctic modifies the allocation of zonal momentum. This is consistent with the Arctic sea-ice reduction exciting a modulation of the AO/NAM as an indirect influence.

Petoukhov and Semenov [2010] showed the strong non-linearity of the linkage between the sea-ice reduction in the Barents-Kara Sea and the associated AO/NAM signals. For example, the intermediate amount of sea-ice reduction observed in recent years induces a negative AO. However, either smaller or larger reductions in sea ice might induce a positive AO through non-linear response to surface heat sources. This is critical to our results as it is difficult to infer future projections of NH climate change from a continuous decline in Arctic sea ice. It is unclear which phase of the AO would be more dominant in the far future after complete sea-ice loss.

4.4. Seasonal Evolution

Our results from both observations and model simulations indicate a transition of the atmospheric response to sea-ice reduction. That is, the anomalous signature of the negative annular mode pattern increases gradually from early winter toward late winter (Figures 3, 4, and 14). The upward surface heat flux associated with the sea-ice reduction in the Barents and Kara Seas strengthens as the season advances from late summer to mid-winter, and the heat flux forces the atmosphere continuously during winter. The climatological waveguide for Rossby wave propagation is located close to the Barents Sea during winter (Figure 9). Due to this continuous forcing, the negative AO-like anomalies evolve from autumn to mid-winter (Figure 14). Furthermore, the model results show a negative NAO-like pattern in the late winter that is linked to the weakening of the polar vortex in the stratosphere (Figures 14 and 15), which suggests a downward influence of stratospheric variability on the troposphere. The day-to-day evolution of the responses has an intra-seasonal timescale (Figure 15), even though our model results are based on the averages of 60 members. Thus, to understand the role of the stratosphere and the stratosphere-troposphere coupling, it is necessary to analyze the anomalies on an intra-seasonal timescale. Previous studies have also suggested stratospheric influence as a possible mechanism for the teleconnection between the variations in tropical SST and the NAO [Scaife *et al.*, 2005; Cagnazzo and Manzini, 2009]. Takaya and Nakamura [2008] pointed out the importance of fluctuations of planetary waves in November

to the annular mode in mid-winter through modulation of the stratospheric polar vortex. It is thus not unrealistic to consider a possible link between sea-ice reduction and the negative phase shift of the NAO in late winter via the stratospheric pathway. However, given its complexity, the topic of a climatic link between the Arctic, the tropics, and the stratosphere is beyond the scope of this study, and the roles of the stratosphere in the seasonal evolution of the climate impacts of sea-ice reduction will be studied in the future.

5. Summary

We used AGCM experiments to investigate the impacts of sea-ice reduction on NH climate and have demonstrated that, in early winter, sea-ice reduction in the Barents Sea causes tropospheric cyclonic anomalies and associated surface cooling anomalies in eastern Siberia. Moreover, the planetary wave modified in mid-latitudes induces an anomalous meridional circulation that shifts the AO/NAM-like pattern more toward the negative phase. The polar vortex in the stratosphere, weakened by a modulation of the planetary wave, couples with the tropospheric responses in the North Atlantic, and thus, negative NAO-like responses appear in late winter. Quantitative estimates derived from our model results showed that atmospheric feedback from the sea-ice reduction induces a heating rate that is equivalent to 63% of the heat release from the ocean into the polar atmosphere due to the sea-ice reduction itself. Associated with the negative AO/NAM-like circulation, near-surface temperature anomalies indicate warm Arctic and cold mid-latitude conditions. This implies a broad influence of the variability of the Arctic ice extent on climate. Probability density function analysis showed that the frequency of a strong negative (positive) AO/NAM is more than doubled (halved) because of recent ice reductions. Our analysis of the ERA interim reanalysis dataset supports this negative phase shift of the AO/NAM. Our results also imply some contribution from Arctic sea-ice reduction to the severe cold weather outbreaks experienced in the NH mid-latitudes in recent years.

The recent atmospheric circulation changes in the real world reflect not only the impact of sea-ice reduction, but also the impacts of decadal and interannual variations in SST, aerosols, ozone, and solar heating. In particular, tropical SST variations have a large effect. To estimate the climatic impact of sea-ice reduction more accurately, a quantitative estimate of the uncertainty associated with the impact of variability in other climate processes is required. As an extension to the present study, we plan to perform ensemble-based GCM experiments in which historical external conditions are used for the recent period (e.g., from 1979 to the present).

Appendix A: Model Performance of Turbulent Heat Fluxes in the Arctic Ocean

As an example of the model performance of the turbulent heat flux, we examine the relationship between the sea-ice thickness in the Arctic Ocean and the climatology of the simulated turbulent heat flux of the *CNTL* run (Figure A1). The 60-year average of the turbulent heat flux in January is from -15 to $+5 \text{ W m}^{-2}$ over the grid with sea ice of more than 30 cm thickness and from $+150$ to $+400 \text{ W m}^{-2}$ over the grid with no ice (i.e., open water). Thus, the simulated heat flux in the Arctic is consistent with the heat flux obtained by observation-based estimation [Maykut, 1982; Renfrew *et al.*, 2002] as mentioned in section 2.4. The consistency between the observation and simulation results strongly supports that the turbulent heat flux over sea ice thicker than 30–50 cm does not change so much because of the large reduction in the conductive heat flux.

Appendix B: Estimation of the Heating Rate due to Residual Mean Vertical Motion

We estimate the heating rate associated with the residual mean vertical motion (w^*) obtained from our TEM analysis. First, we calculate potential temperature advection due to the vertical motion, as follows:

$$\left[\frac{\partial \theta}{\partial t} \right] = -(w^*)' \frac{\partial \bar{\theta}}{\partial z^*} \quad (\text{B1})$$

where θ is potential temperature, w^* is the residual mean vertical velocity, $z^* = -H \log(p/p_0)$ (where H is the scale height (assumed to be 7 km), p and p_0 are the pressures at a given level and the surface pressure (1000 hPa), respectively), $()'$ indicates a 3-month average anomaly (*N.ICE* minus *CNTL*), and an overbar indicates the climatology of the respective 3-month averages, which are defined as 120-year averages of *CNTL* and *N.ICE*.

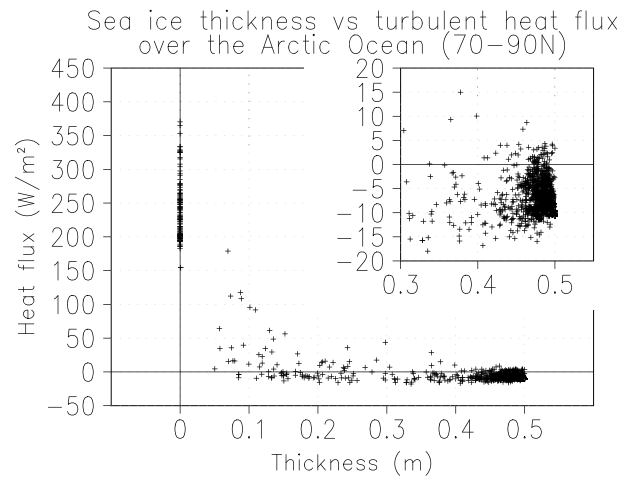


Figure A1. Scatter diagram showing the sea-ice thickness in each of grid over the Arctic Ocean (northward of 70°N, excluding land) and the climatology (i.e., 60 years average of CNTL run) of turbulent heat flux (i.e., sensible and latent heat fluxes) in January. A panel in the top-right corner is of vertically enlarged diagram for the sea-ice thickness greater than 0.3 m.

We ignore second-order terms of the potential temperature advection because fluctuations in the vertical gradient of the potential temperature are smaller than its climatological average.

We obtain the heating rate per unit mass as follows:

$$Q^* = Cp(p/p_0)^\kappa \left[\frac{\partial \theta}{\partial t} \right] \quad (B2)$$

where Cp is the specific heat at constant pressure and κ is the Poisson constant. Finally, for comparison with the turbulent heat flux due to ice reduction, we obtain the heating rate per unit area from vertical integration of Q^* between 850 and 300 hPa:

$$J = \frac{1}{g} \int_{p=850 \text{ hPa}}^{p=300 \text{ hPa}} Q^* dp \quad (B3)$$

where g is gravitational acceleration; thus, J indicates the dynamical heating rate over the free troposphere.

Acknowledgments

Merged Hadley-NOAA/OI SST and SIC data were obtained from the Climate Data Guide provided by the National Center for Atmospheric Research (NCAR) and University Corporation for Atmospheric Research (UCAR) (<https://climatedataguide.ucar.edu/>). The ERA interim data were obtained from the ECMWF website (<http://data-portal.ecmwf.int/>). The AFES simulations were performed on the Earth Simulator at the Japan Agency for Marine-Earth Science and Technology (JAMSTEC). To access our AFES simulation data, contact the corresponding author (nakamura.tetsu@ees.hokudai.ac.jp). We thank the AFES development team at JAMSTEC and the Nakamura laboratory team at the University of Tokyo for their help in setting up and tuning the AFES simulations. We also thank K. Dethloff, D. Handorf, R. Jaiser, K. Nishii, K. Takaya, and A. Kuwano-Yoshida for helpful discussions and comments. This study was supported by the Green Network of Excellence Program (GRENE Program) Arctic Climate Change Research Project and the Japanese Ministry of Education, Culture, Sports, Science and Technology (MEXT) through a Grant-in-Aid for Scientific Research in Innovative Areas 2205.

References

Alexander, M. A., U. S. Bhatt, J. E. Walsh, M. S. Timlin, J. S. Miller, and J. D. Scott (2004), The atmospheric response to realistic Arctic sea ice anomalies in an AGCM during winter, *J. Clim.*, *17*, 890–905.

Ambaum, M. H. P., and B. Hoskins (2002), The NAO troposphere-stratosphere connection, *J. Clim.*, *15*, 1969–1978.

Andrews, D. G., and M. E. McIntyre (1976), Planetary waves in horizontal and vertical shear: The generalized Eliassen-Palm relation and the mean zonal acceleration, *J. Atmos. Sci.*, *33*, 2031–2048.

Baldwin, M. P., and T. J. Dunkerton (1999), Downward propagation of the Arctic Oscillation from the stratosphere to the troposphere, *J. Geophys. Res.*, *104*(D24), 30,937–30,946, doi:10.1029/1999JD900445.

Baldwin, M. P., and T. J. Dunkerton (2001), Stratospheric harbingers of anomalous weather regimes, *Science*, *294*, 581–584, doi:10.1126/science.1063315.

Cagnazzo, C., and E. Manzini (2009), Impact of the stratosphere on the winter tropospheric teleconnections between ENSO and the North Atlantic and European region, *J. Clim.*, *22*, 1223–1238.

Cohen, J. L., J. C. Furtado, M. A. Barlow, V. A. Alexeev, and J. E. Cherry (2012), Arctic warming, increasing snow cover and widespread boreal winter cooling, *Environ. Res. Lett.*, *7*, 014007, doi:10.1088/1748-9326/7/1/014007.

Comiso, J. C., C. L. Parkinson, R. Gersten, and L. Stock (2008), Accelerated decline in the Arctic sea ice cover, *Geophys. Res. Lett.*, *35*, L01703, doi:10.1029/2007GL031972.

Dee, D. P., et al. (2011), The ERA-interim reanalysis: Configuration and performance of the data assimilation system, *Q. J. R. Meteorol. Soc.*, *137*, 553–597, doi:10.1002/qj.828.

Deser, C., and A. S. Phillips (2009), Atmospheric circulation trends, 1950–2000: The relative roles of sea surface temperature forcing and direct atmospheric radiative forcing, *J. Clim.*, *22*, 396–413, doi:10.1175/2008JCLI2453.1.

Deser, C., G. Magnusdottir, R. Saravanan, and A. Phillips (2004), The effects of North Atlantic SST and sea ice anomalies on the winter circulation in CCM3. Part II: Direct and indirect components of the response, *J. Clim.*, *17*, 877–889.

Enomoto, T., A. Kuwano-Yoshida, N. Komori, and W. Ohfuchi (2008), Description of AFES 2: Improvements for high-resolution and coupled simulations, in *High Resolution Numerical Modelling of the Atmosphere and Ocean*, edited by K. Hamilton and W. Ohfuchi, pp. 77–97, Springer, New York.

Francis, J. A., W. Chan, D. J. Leathers, J. R. Miller, and D. E. Veron (2009), Winter Northern Hemisphere weather patterns remember summer Arctic sea ice extent, *Geophys. Res. Lett.*, *36*, L07503, doi:10.1029/2009GL037274.

Holland, M. M., C. M. Bitz, L.-B. Tremblay, and D. A. Bailey (2008), The role of natural versus forced change in future rapid summer Arctic ice loss, in *Arctic Sea Ice Decline: Observations, Projections, Mechanisms, and Implications*, *Geophys. Monogr.*, vol. 180, edited by E. T. DeWeaver, C. M. Bitz, and L.-B. Tremblay, pp. 133–150, AGU, Washington, D. C.

Honda, M., K. Yamazaki, Y. Tachibana, and K. Takeuchi (1996), Influence of Okhotsk sea-ice extent on atmospheric circulation, *Geophys. Res. Lett.*, *23*, 3595–3598, doi:10.1029/96GL03474.

Honda, M., K. Yamazaki, H. Nakamura, and K. Takeuchi (1999), Dynamic and thermodynamic characteristics of atmospheric response to anomalous sea-ice extent in the Sea of Okhotsk, *J. Clim.*, *12*, 3347–3358.

Honda, M., J. Inoue, and S. Yamane (2009), Influence of low Arctic sea-ice minima on anomalously cold Eurasian winters, *Geophys. Res. Lett.*, *36*, L08707, doi:10.1029/2008GL037079.

Hopsch, S., J. Cohen, and K. Dethloff (2012), Analysis of a link between fall Arctic sea ice concentration and atmospheric patterns in the following winter, *Tellus A*, *64*, 18624, doi:10.3402/tellusa.v64i0.18624.

Hurrell, J. W., J. J. Hack, D. Shea, J. M. Caron, and J. Rosinski (2008), A new sea surface temperature and sea ice boundary dataset for the Community Atmosphere Model, *J. Clim.*, *21*, 5145–5153.

- Inoue, J., M. E. Hori, and K. Takaya (2012), The role of Barents Sea ice in the wintertime cyclone track and emergence of a warm-Arctic cold-Siberian anomaly, *J. Clim.*, *25*, 2561–2568, doi:10.1175/JCLI-D-11-00449.1.
- Jaiser, R., K. Dethloff, D. Handorf, A. Rinke, and J. Cohen (2012), Impact of sea ice cover changes on the Northern Hemisphere atmospheric winter circulation, *Tellus A*, *64*, 11595, doi:10.3402/tellusa.v64i0.11595.
- Kay, J. E., M. M. Holland, and A. Jahn (2011), Inter-annual to multi-decadal Arctic sea ice extent trends in a warming world, *Geophys. Res. Lett.*, *38*, L15708, doi:10.1029/2011GL048008.
- Kim, B.-M., et al. (2014), Weakening of the stratospheric polar vortex by Arctic sea-ice loss, *Nat. Commun.*, *5*, 4646, doi:10.1038/ncomms5646.
- Kimoto, M., and M. Ghil (1993), Multiple flow regimes in the Northern Hemisphere winter. Part I: Methodology and hemispheric regimes, *J. Atmos. Sci.*, *50*, 2625–2643.
- Kuwano-Yoshida, A., T. Enomoto, and W. Ohfuchi (2010), An improved PDF cloud scheme for climate simulations, *Q. J. R. Meteorol. Soc.*, *136*, 1583–1597.
- L'Heureux, M. L., A. Kumar, G. D. Bell, M. S. Halpert, and R. W. Higgins (2008), Role of the Pacific-North American (PNA) pattern in the 2007 Arctic sea ice decline, *Geophys. Res. Lett.*, *35*, L20701, doi:10.1029/2008GL035205.
- Lau, N. C., and E. O. Holopainen (1984), Transient eddy forcing of the time-mean flow as identified by geopotential tendencies, *J. Atmos. Sci.*, *41*, 313–328.
- Lau, N.-C., and M. J. Nath (1991), Variability of the baroclinic and barotropic transient eddy forcing associated with monthly changes in the midlatitude storm tracks, *J. Atmos. Sci.*, *48*, 2589–2613.
- Limpasuvan, V., and D. L. Hartmann (2000), Wave-maintained annular modes of climate variability, *J. Clim.*, *13*, 4414–4429.
- Liu, J.-P., J. A. Curry, H. Wang, M. Song, and R. M. Horton (2012), Impact of declining Arctic sea ice on winter snowfall, *Proc. Natl. Acad. Sci. U.S.A.*, *109*, 4074–4079, doi:10.1073/pnas.1114910109.
- Magnusdottir, G., C. Deser, and R. Saravanan (2004), The effects of North Atlantic SST and sea-ice anomalies on the winter circulation in CCM3. Part I: Main features and storm-track characteristics of the response, *J. Clim.*, *17*, 857–876.
- Maslanik, J., S. Drobot, C. Fowler, W. Emery, and R. Barry (2007), On the Arctic climate paradox and the continuing role of atmospheric circulation in affecting sea ice conditions, *Geophys. Res. Lett.*, *34*, L03711, doi:10.1029/2006GL028269.
- Maykut, G. A. (1982), Large-scale heat exchange and ice production in the central Arctic, *J. Geophys. Res.*, *87*, 7971–7984, doi:10.1029/JC087iC10p07971.
- Mori, M., M. Watanabe, H. Shigeo, J. Inoue, and M. Kimoto (2014), Robust Arctic sea-ice influence on the frequent Eurasian cold winters in past decades, *Nat. Geosci.*, *7*, 869–873, doi:10.1038/ngeo2277.
- Ogi, M., and K. Yamazaki (2010), Trends in the summer Northern Annular Mode and Arctic sea ice, *Sci. Online Lett. Atmos.*, *6*, 41–44, doi:10.2151/sola.2010-011.
- Ogi, M., I. G. Rigor, M. G. McPhee, and J. M. Wallace (2008), Summer retreat of Arctic sea ice: Role of summer winds, *Geophys. Res. Lett.*, *35*, L24701, doi:10.1029/2008GL035672.
- Ogi, M., K. Yamazaki, and J. M. Wallace (2010), Influence of winter and summer surface wind anomalies on summer Arctic sea ice extent, *Geophys. Res. Lett.*, *37*, L07701, doi:10.1029/2009GL042356.
- Ohfuchi, W., H. Nakamura, M. K. Yoshioka, T. Enomoto, K. Takaya, X. Peng, S. Yamane, T. Nishimura, Y. Kurihara, and K. Ninomiya (2004), 10-km mesh meso-scale resolving simulations of the global atmosphere on the Earth Simulator—Preliminary outcomes of AFES (AGCM for the Earth Simulator), *J. Earth Simul.*, *1*, 8–34.
- Ohfuchi, W., H. Sasaki, Y. Masumoto, and H. Nakamura (2007), “Virtual” atmospheric and oceanic circulation in the Earth Simulator, *Bull. Am. Meteorol. Soc.*, *88*, 861–866.
- Ohhashi, Y., and K. Yamazaki (1999), Variability of the Eurasian pattern and its interpretation by wave activity flux, *J. Meteorol. Soc. Jpn.*, *77*, 495–511.
- Onogi, K., et al. (2007), The JRA-25 reanalysis, *J. Meteorol. Soc. Jpn.*, *85*, 369–432, doi:10.2151/jmsj.85.369.
- Overland, J. E., and M. Wang (2010), Large-scale atmospheric circulation changes are associated with the recent loss of Arctic sea ice, *Tellus A*, *62*, 1–9, doi:10.1111/j.1600-0870.2009.00421.x.
- Petoukhov, V., and V. A. Semenov (2010), A link between reduced Barents-Kara sea ice and cold winter extremes over northern continents, *J. Geophys. Res.*, *115*, D21111, doi:10.1029/2009JD013568.
- Polvani, L. M., and D. W. Waugh (2004), Upward wave activity flux as a precursor to extreme stratospheric events and subsequent anomalous surface weather regimes, *J. Clim.*, *17*, 3548–3554.
- Renfrew, I. A., G. W. K. Moore, P. S. Guest, and K. Bumke (2002), A comparison of surface layer and surface turbulent flux observations over the Labrador Sea with ECMWF analyses and NCEP reanalyses, *J. Phys. Oceanogr.*, *32*, 383–400.
- Rigor, I. G., R. L. Colony, and S. Martin (2000), Variations in surface air temperature observations in the Arctic, 1979–97, *J. Clim.*, *13*, 896–914.
- Rigor, I. G., J. M. Wallace, and R. L. Colony (2002), Response of sea ice to the Arctic Oscillation, *J. Clim.*, *15*, 2648–2663.
- Rinke, A., K. Dethloff, W. Dorn, D. Handorf, and J. C. Moore (2013), Simulated Arctic atmospheric feedbacks associated with late summer sea ice anomalies, *J. Geophys. Res. Atmos.*, *118*, 7698–7714, doi:10.1002/jgrd.50584.
- Scaife, A. A., J. R. Knight, G. K. Vallis, and C. K. Folland (2005), A stratospheric influence on the winter NAO and North Atlantic surface climate, *Geophys. Res. Lett.*, *32*, L18715, doi:10.1029/2005GL023226.
- Schweiger, A. J., R. W. Lindsay, S. Vavrus, and J. A. Francis (2008), Relationships between Arctic sea ice and clouds during autumn, *J. Clim.*, *21*, 4799–4810.
- Screen, J. A., I. Simmonds, C. Deser, and R. Tomas (2013), The atmospheric response to three decades of observed Arctic Sea ice loss, *J. Clim.*, *26*, 1230–1248, doi:10.1175/JCLI-D-12-00063.1.
- Serreze, M. C., M. M. Holland, and J. Stroeve (2007), Perspectives on the Arctic's shrinking sea ice cover, *Science*, *315*, 1533–1536.
- Serreze, M. C., A. P. Barrett, J. C. Stroeve, D. N. Kindig, and M. M. Holland (2009), The emergence of surface-based Arctic amplification, *Cryosphere*, *3*, 11–19.
- Sokolova, E., K. Dethloff, A. Rinke, and A. Benkel (2007), Planetary and synoptic scale adjustment of the Arctic atmosphere to sea ice cover changes, *Geophys. Res. Lett.*, *34*, L17816, doi:10.1029/2007GL030218.
- Stroeve, J. C., M. C. Serreze, M. M. Holland, J. E. Kay, J. Malanik, and A. P. Barrett (2011), The Arctic's rapidly shrinking sea ice cover: A research synthesis, *Clim. Change*, *110*, 1005–1027, doi:10.1007/s10584-011-0101-1.
- Stroeve, J., M. M. Holland, W. Meier, T. Scambos, and M. Serreze (2007), Arctic sea ice decline: Faster than forecast, *Geophys. Res. Lett.*, *24*, L09501, doi:10.1029/2007GL029703.
- Takaya, K., and H. Nakamura (2001), A formulation of a phase-independent wave-activity flux for stationary and migratory quasigeostrophic eddies on a zonally varying basic flow, *J. Atmos. Sci.*, *58*, 608–627.
- Takaya, K., and H. Nakamura (2008), Precursory changes in planetary wave activity for midwinter surface pressure anomalies over the Arctic, *J. Meteorol. Soc. Jpn.*, *86*, 415–427.

- Tang, Q., X. Zhang, X. Yang, and J. A. Francis (2013), Cold winter extremes in northern continents linked to Arctic sea ice loss, *Environ. Res. Lett.*, *8*, 014036, doi:10.1088/1748-9326/8/1/014036.
- Thompson, D. W. J., and J. M. Wallace (1998), The Arctic Oscillation signature in the wintertime geopotential height and temperature fields, *Geophys. Res. Lett.*, *25*, 1297–1300, doi:10.1029/98GL00950.
- Thompson, D. W. J., and J. M. Wallace (2000), Annular modes in the extratropical circulation. Part I: Month-to-month variability, *J. Clim.*, *13*, 1000–1016.
- Wallace, J. M., and D. S. Gutzler (1981), Teleconnections in the geopotential height field during the Northern Hemisphere winter, *Mon. Weather Rev.*, *109*, 784–812.
- Wang, M., and J. E. Overland (2009), A sea ice free summer Arctic within 30 years?, *Geophys. Res. Lett.*, *36*, L07502, doi:10.1029/2009GL037820.
- Wu, B., J. Wang, and J. E. Walsh (2006), Dipole anomaly in the winter Arctic atmosphere and its association with sea ice motion, *J. Clim.*, *19*, 210–225.
- Yamamoto, K., Y. Tachibana, M. Honda, and J. Ukita (2006), Intra-seasonal relationship between the Northern Hemisphere sea ice variability and the North Atlantic Oscillation, *Geophys. Res. Lett.*, *33*, L14711, doi:10.1029/2006GL026286.